



# Seasonal Pattern of Tidal-Flat Topography along the Jiangsu Middle Coast, China, Using HJ-1 Optical Images

Yongxue Liu · Manchun Li · Liang Mao · Liang Cheng · Kefeng Chen

Received: 11 March 2013 / Accepted: 11 June 2013 / Published online: 27 June 2013  
© Society of Wetland Scientists 2013

**Abstract** Seasonal topographical changes in the intertidal zone are of high interest in many parts of the world. Due to existing challenges in mapping this dynamics, little is known about the seasonal pattern of tidal flats. This research aims to fill the knowledge gap by using optical images from the Chinese HJ-1 satellites constellation. A case study was conducted at the Jiangsu middle coast, a typical tidal flat region in China. Firstly, 455 optical images from the HJ-1 Satellites were collected to construct seasonal tidal flat Digital Elevation Models (DEMs). Next, synchronous Light Detection and Ranging (LiDAR) DEM and ground survey data were collected to validate the accuracy of the

seasonal tidal flat DEMs. Finally, seasonal pattern of the tidal flats was demonstrated based on a time series of DEM volume comparison. The results show: (1) the HJ-1 images are qualified data source to produce satisfactory tidal flat DEMs with high spatio-temporal resolution and acceptable vertical accuracy. (2) In general, there are apparent erosion-and-deposition cycles in the Jiangsu middle coast, with deposition during the Winter and erosion during the Summer. Furthermore, the derived seasonal patterns differ notably among the five major sandbanks.

**Keywords** Tidal flats · Coastal morphology · Digital elevation model · Seasonal pattern · HJ-1 satellites constellation

---

Y. X. Liu (✉)  
Jiangsu Provincial Key Laboratory of Geographic Information Science and Technology, Nanjing University, Nanjing, Jiangsu Province 210093, People's Republic of China  
e-mail: yongxue@nju.edu.cn

M. C. Li  
School of Geographic and Oceanographic Sciences, Nanjing University, Nanjing, Jiangsu Province 210093, People's Republic of China  
e-mail: manchun@nju.edu.cn

L. Mao  
Department of Geography, University of Florida, Gainesville, FL 32611, USA  
e-mail: liangmao@ufl.edu

L. Cheng  
Department of Geographic Information Science, Nanjing University, Nanjing, Jiangsu Province 210093, People's Republic of China  
e-mail: lcheng@nju.edu.cn

K. F. Chen  
Nanjing Hydraulic Research Institute, Nanjing, Jiangsu Province 210093, People's Republic of China  
e-mail: chenkefengnju@163.com

## Introduction

Tidal flats (also known as the intertidal zones) are areas between the mean high tide and mean low tide levels (Chen et al. 2008). Shaped by tides, waves, and other sedimentary factors, the topography of tidal flats is highly dynamic over time and space, exhibiting a cyclic pattern between seasons (Lemke et al. 2009; Pino et al. 1999). An understanding of this seasonal pattern is critical to the ecosystem, socio-economy, and sustainability of coastal areas, e.g. wildlife habitats management, land reclamation planning, and storm surges prevention (Wang et al. 2012b).

In the current literature, however, little is known about the seasonal pattern of tidal flat, although its importance has been widely recognized (Chen et al. 2008). This issue can be attributed to the varying topography of tidal flat and the resultant difficulties in acquiring highly resolved spatio-temporal information. The traditional method through ground-based or aerial surveys is almost impractical to

satisfy the needs of high temporal resolution data due to expensive costs (Chen and Rau 1998; Wimmer et al. 2000; Woolard and Colby 2002). The well-accepted Waterline Detection Method (WDM) (Mason et al. 1995) could effectively construct Digital Elevation Models (DEMs) for tidal flats at low costs (Mason et al. 1998; Lohani and Mason 1999; Liu et al. 2010; Mason et al. 2000; Blott and Pye 2004; Zhao et al. 2008; Heygster et al. 2010; Mason et al. 2010). The WDM produced DEMs possess sufficient spatial resolution (30–60 m) and vertical accuracy ( $\sim 40$  cm), but the temporal resolution is often longer than one year and thus too coarse to detect seasonal pattern of tidal flats (Ryu et al. 2008; Zhao et al. 2008; Liu et al. 2012). Poor temporal continuity limits the analysis of seasonal patterns as well as inter-annual patterns. New data, methods, technologies, and studies are called for to fill this knowledge gap.

This study attempts to analyze the seasonal pattern of tidal flat topography along the Jiangsu coast using newly published optical images from the “Chinese environment and disaster monitoring and forecasting with a small satellite constellation”, hereinafter referred to as the HJ-1 satellites constellation. Specifically, three objectives of this research are to (1) analyze the feasibility of the HJ-1 images to create seasonal tidal flat DEMs; (2) validate the vertical accuracy of the DEMs obtained at relatively short time intervals; and (3) quantitatively describe the seasonal patterns of tidal-flat topography based on the obtained DEMs.

## Materials and Methods

### Study Area

The Jiangsu middle coast is ranging from the mouth of Xinyang Port in the north to Xiaoyangkou Port in the south (Fig. 1). Its offshore area is located the South Yellow Sea Radial Sand Ridges (SYSRSR)—the largest tidal sand ridges on the Chinese continental shelf. The SYSRSR consist of more than 10 large linear submarine sand ridges and have a very unique radial fan shape (Wang et al. 2012a). The muddy tidal flats are even and wide, with a typical width of 4 to 8 km, while the widest one is almost 25 km. The area of the tidal flats above the Lowest Normal Low Water (LNLW) level in Jiangsu middle coast exceeds 2,800 km<sup>2</sup> (including the SYSRSR). The Jiangsu middle coast has an irregular semidiurnal tide with a mean tide range varying from 2.5 to 4.0 m (Xing et al. 2012). The largest mean tide range on the Jiangsu middle coast exists in the section from Jianggang Port to Xiaoyangkou Port, and the mean tide range decreases gradually as it is away along the coast (Liu et al. 2011). The Jiangsu middle coast has a maritime monsoon climate ranging from warm-temperate to northern subtropical (Zhang and Chen 1992). Seasonal changes are quite well defined, with

each season lasting approximately three months (Spring: March to May; Summer: June to August; Autumn: September to November; and Winter: December to February). February has the minimum air temperature ranging from  $-1.5$  to  $2.5$  °C, while the highest air temperature happens in August varying from  $26.5$  to  $27.5$  °C (Zhou et al. 2009). The summer (especially for June and July) weather tends to be wet and cloudy resulted from the Jiang-huai quasi-stationary front.

### Data Collection

- (1) **Ground-survey data.** Six transects (magenta and yellow points in Fig. 1) were measured in high water using a combination of vessel-based echo sounding and Real Time Kinematic (RTK) GPS. Three of the transects ( $T_1$ ,  $T_2$ ,  $T_3$ ) were measured in April and May 2008, while the other three transects ( $T_4$ ,  $T_5$ ,  $T_6$ ) were measured in October 2008. The length of the six transects is 1,850 m, 4,060 m, 3,000 m, 2,300 m, 13,760 m, 8,050 m, respectively. All transects data were sampled at approximately 15-m intervals, which were used to determine the accuracy of produced DEMs in the corresponding time-period.
- (2) **Airborne elevation data.** Airborne Light Detection and Ranging (LiDAR) data were collected in April and May of 2006 by Jiangsu Provincial Bureau of Surveying, Mapping and Geo-information. The spacing of original LiDAR points was set to 1 m, and the vertical error of LiDAR DEMs was less than 10 cm (GPS-RTK synchronous validation along Jiangsu coast). The LiDAR DEMs provided to the research team had a vertical accuracy of less than 15 cm and were resampled to a  $5 \times 5$  m grid. In combination with the ground survey data, the LiDAR-derived data were also used to determine the accuracy of the DEMs in the corresponding time-period.
- (3) **HJ-1 images.** The HJ-1 satellites constellation consists of three satellites: HJ-1 A and B (launched on September 6, 2008); and HJ-1 C (launched on November 19, 2012, currently on-orbit test) (Wang 2012). HJ-1 A and B satellites each carries two wide-coverage Charge Coupled Device (CCD) sensors. The two CCD sensors carried by each satellite form a combined 700 km width ground swath. In addition, HJ-1 A and B were placed in the same orbital plane with a  $180^\circ$  phase difference, producing optical images of 30 m resolution, covering China and the surrounding areas at intervals of less than 48 h (Wang et al. 2010; Cai et al. 2011). A total of 455 phases of HJ-1 images covering the Jiangsu middle coast were obtained, covering the period from November 2008 to December 2010 (Table 1). Images were downloaded

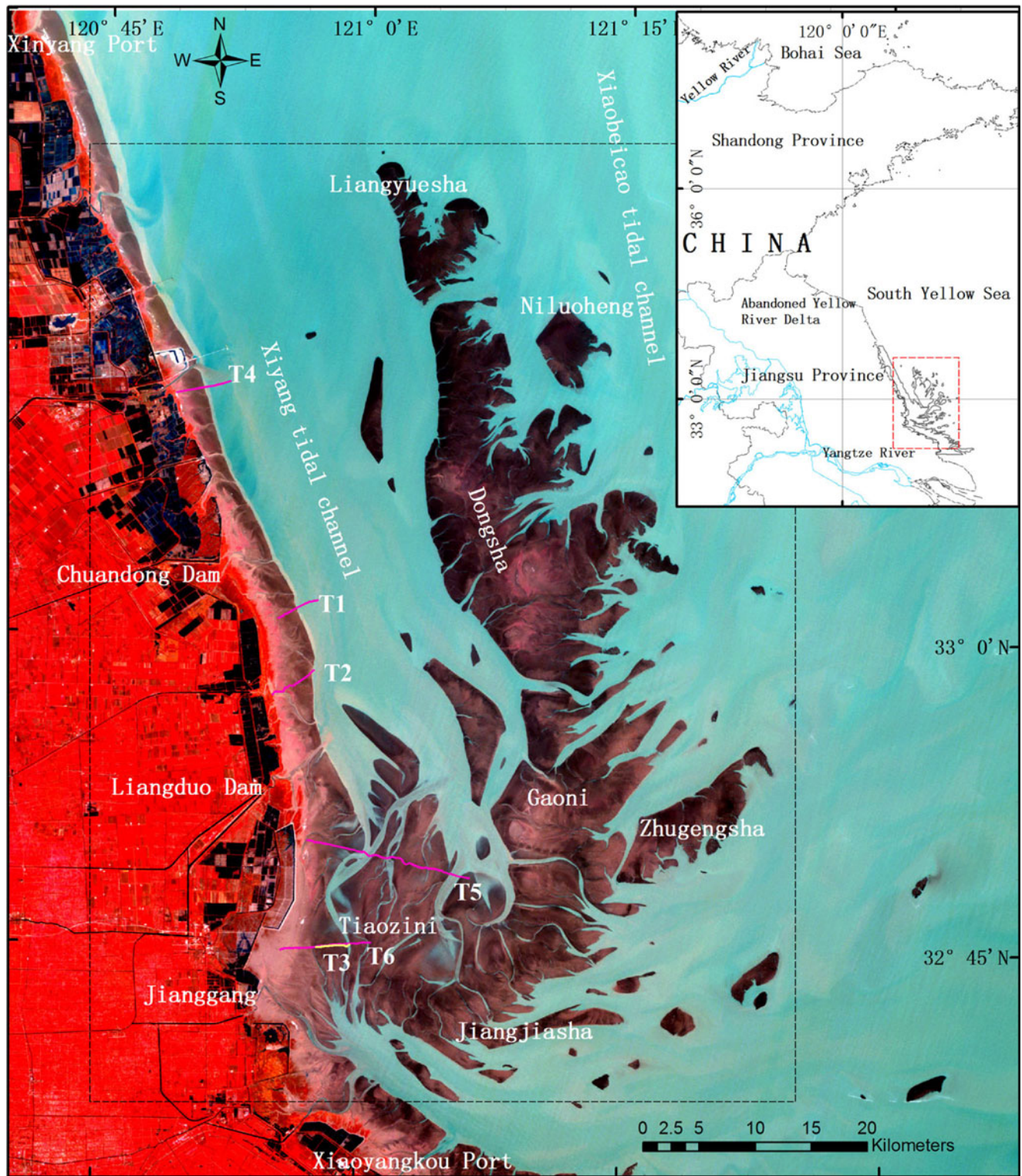


Fig. 1 HJ-1B image of the Jiangsu middle coast (R4G3B2, GMT 02:41, December 22, 2009)

from the China Center for Resource Satellite Data and Applications (CRESDA, <http://www.cresda.com>).

(4) *Medium-resolution satellite images.* Another 25 non HJ-1 images taken at the same time-period as the

airborne LiDAR data (March to May 2006) and the ground survey data (March to May and October to December 2008) were collected. These satellite images were obtained from different platforms, including

**Table 1** Summary of HJ-1 and medium-resolution satellite images used in this study

No.	Sensor	Acquired time <sup>a</sup> yy-mm-dd hh:ss	Height <sup>b</sup> (cm)	No.	Sensor	Acquired time <sup>a</sup> yy-mm-dd hh:ss	Height <sup>b</sup> (cm)	No.	Sensor	Acquired time <sup>a</sup> yy-mm-dd hh:ss	Height <sup>b</sup> (cm)
1	CBERS CCD	2006-03-03 02:33	-198.7	46	HJ-1B CCD	2009-02-10 02:35	-86.6	91	HJ-1A CCD	2009-08-14 02:47	-42.8
2	CBERS CCD	2006-03-29 02:32	49.3	47	HJ-1A CCD	2009-02-12 02:36	-229.5	92	HJ-1B CCD	2009-08-16 02:50	109.4
3	ERS-2 SAR	2006-04-02 02:33	-191.0	48	HJ-1B CCD	2009-02-14 02:38	-213.9	93	HJ-1A CCD	2009-08-18 02:50	232.7
4	BJ-1 CCD	2006-04-02 02:18	-185.5	49	HJ-1A CCD	2009-02-20 02:42	68.7	94	HJ-1A CCD	2009-08-22 02:53	-78.8
5	ERS SAR	2006-04-17 14:14	-148.9	50	HJ-1B CCD	2009-03-06 02:53	48.8	95	HJ-1A CCD	2009-08-26 02:56	-176.5
6	CBERS CCD	2006-04-24 02:32	195.9	51	HJ-1B CCD	2009-03-14 02:59	-205.8	96	HJ-1B CCD	2009-08-28 02:58	-82.1
7	EO-1 ALI	2006-05-03 02:12	-158.5	52	HJ-1A CCD	2009-03-15 02:35	-212.0	97	HJ-1A CCD	2009-09-03 03:01	166.4
8	SPOT HRV	2006-05-03 02:30	-171.2	53	HJ-1B CCD	2009-03-17 02:36	-181.8	98	HJ-1B CCD	2009-09-04 02:39	69.2
9	IRS-P6 LISS	2006-05-03 02:45	-179.8	54	HJ-1B CCD	2009-03-18 03:02	-124.7	99	HJ-1A CCD	2009-09-06 02:39	-63.0
10	ERS SAR	2006-05-07 02:33	71.2	55	HJ-1A CCD	2009-03-20 03:03	-49.7	100	HJ-1A CCD	2009-09-07 03:04	-65.2
11	BJ-1 CCD	2006-05-21 02:21	49.3	56	HJ-1A CCD	2009-03-24 03:06	176.4	101	HJ-1B CCD	2009-10-02 02:58	204.5
12	EO-1 ALI	2006-05-28 02:18	-121.5	57	HJ-1B CCD	2009-03-25 02:42	123.6	102	HJ-1A CCD	2009-10-04 02:58	161.8
13	LandSat TM	2006-05-29 02:23	-162.0	58	HJ-1B CCD	2009-04-02 02:48	-122.3	103	HJ-1B CCD	2009-10-06 03:01	20.5
14	IRS-P6 LISS	2008-03-05 02:43	154.6	59	HJ-1B CCD	2009-04-06 02:51	205.8	104	HJ-1A CCD	2009-10-08 03:01	-123.9
15	IRS-P6 AWiFS	2008-03-10 02:39	-188.7	60	HJ-1A CCD	2009-04-08 02:53	218.8	105	HJ-1B CCD	2009-10-10 03:04	-114.5
16	CBERS CCD	2008-03-14 02:51	-117.3	61	HJ-1A CCD	2009-04-15 02:33	-186.1	106	HJ-1A CCD	2009-10-15 02:42	230.4
17	IRS-P6 AWiFS	2008-03-24 02:46	-176.0	62	HJ-1B CCD	2009-04-17 02:35	-120.6	107	HJ-1B CCD	2009-10-17 02:44	235.3
18	EO-1 ALI	2008-04-17 02:23	214.0	63	HJ-1B CCD	2009-04-18 03:00	-81.7	108	HJ-1B CCD	2009-10-21 02:47	-109.4
19	CBERS CCD	2008-04-23 03:07	-139.1	64	HJ-1B CCD	2009-04-21 02:38	138.7	109	HJ-1A CCD	2009-10-23 02:47	-153.8
20	CBERS CCD	2008-05-02 02:55	184.4	65	HJ-1B CCD	2009-04-22 03:03	182.8	110	HJ-1A CCD	2009-10-31 10:53	-193.9
21	CBERS CCD	2008-05-05 02:51	131.8	66	HJ-1B CCD	2009-04-25 02:41	31.8	111	HJ-1B CCD	2009-11-05 02:33	-100.8
22	IRS-P6 AWiFS	2008-05-06 02:53	21.0	67	HJ-1A CCD	2009-04-27 02:42	-149.3	112	HJ-1B CCD	2009-11-06 02:58	-123.8
23	IRS-P6 AWiFS	2008-05-07 02:33	-129.9	68	HJ-1B CCD	2009-04-29 02:44	-174.0	113	HJ-1B CCD	2009-11-21 02:44	-162.8
24	IRS-P6 AWiFS	2008-05-11 02:49	-138.8	69	HJ-1A CCD	2009-05-01 02:45	-118.7	114	HJ-1A CCD	2009-11-23 02:44	-167.3
25	CBERS CCD	2008-05-31 02:52	147.9	70	HJ-1A CCD	2009-05-05 02:48	200.0	115	HJ-1B CCD	2009-12-03 02:52	46.5
26	CBERS CCD	2008-10-08 02:52	-51.7	71	HJ-1B CCD	2009-05-07 02:50	223.4	116	HJ-1B CCD	2009-12-05 02:52	-155.8
27	HJ-1A CCD	2008-10-27 02:50	223.4	72	HJ-1A CCD	2009-05-09 02:51	29.7	117	HJ-1B CCD	2009-12-07 02:55	-174.7
28	HJ-1A CCD	2008-11-12 03:03	269.0	73	HJ-1B CCD	2009-05-11 02:53	-130.3	118	HJ-1B CCD	2009-12-19 03:03	-127.9
29	HJ-1B CCD	2008-11-21 02:45	4.6	74	HJ-1A CCD	2009-05-13 02:54	-176.7	119	HJ-1A CCD	2009-12-20 02:38	-182.8
30	EO-1 ALI	2008-11-28 02:19	-27.0	75	HJ-1B CCD	2009-05-18 02:34	-18.6	120	HJ-1A CCD	2009-12-21 03:03	-196.0
31	HJ-1B CCD	2008-11-29 02:52	-13.5	76	HJ-1B CCD	2009-05-22 02:36	176.0	121	HJ-1B CCD	2009-12-22 02:41	-194.2
32	HJ-1A CCD	2008-12-05 02:56	-140.4	77	HJ-1A CCD	2009-05-24 02:37	66.5	122	HJ-1A CCD	2009-12-28 02:43	121.7
33	HJ-1B CCD	2008-12-07 02:58	9.2	78	HJ-1B CCD	2009-05-26 02:39	-116.2	123	HJ-1B CCD	2009-12-30 02:46	181.1
34	HJ-1B CCD	2008-12-10 02:36	216.0	79	HJ-1B CCD	2009-06-03 02:45	160.4	124	HJ-1A CCD	2010-01-01 02:46	20.6
35	HJ-1A CCD	2008-12-12 02:37	167.7	80	HJ-1A CCD	2009-06-05 02:46	195.1	125	HJ-1B CCD	2010-01-03 02:49	-187.7

**Table 1** (continued)

No.	Sensor	Acquired time <sup>a</sup> yy-mm-dd hh:ss	Height <sup>b</sup> (cm)	No.	Sensor	Acquired time <sup>a</sup> yy-mm-dd hh:ss	Height <sup>b</sup> (cm)	No.	Sensor	Acquired time <sup>a</sup> yy-mm-dd hh:ss	Height <sup>b</sup> (cm)
36	HJ-1B CCD	2008-12-14 02:39	-64.1	81	HJ-1B CCD	2009-06-11 02:51	-152.2	126	HJ-1A CCD	2010-01-13 02:54	145.5
37	HJ-1B CCD	2008-12-15 03:04	-112.6	82	HJ-1B CCD	2009-06-19 02:57	117.8	127	HJ-1B CCD	2010-01-14 02:32	29.6
38	HJ-1A CCD	2008-12-16 02:41	-169.3	83	HJ-1B CCD	2009-06-23 03:00	73.5	128	HJ-1B CCD	2010-01-18 02:34	-198.4
39	HJ-1B CCD	2008-12-22 02:45	100.0	84	HJ-1A CCD	2009-06-24 02:35	-98.8	129	HJ-1A CCD	2010-01-24 02:36	-39.2
40	HJ-1A CCD	2009-01-01 02:53	-207.4	85	HJ-1A CCD	2009-06-25 03:00	-125.0	130	HJ-1B CCD	2010-01-26 02:40	83.2
41	HJ-1A CCD	2009-01-08 02:34	157.8	86	HJ-1A CCD	2009-07-02 02:41	105.2	131	HJ-1A CCD	2010-01-28 02:39	163.6
42	HJ-1B CCD	2009-01-10 02:35	128.9	87	HJ-1B CCD	2009-07-04 02:43	172.4	132	HJ-1A CCD	2010-01-29 03:04	180.4
43	HJ-1A CCD	2009-01-16 02:40	-200.6	88	HJ-1B CCD	2009-07-20 02:55	205.9	133	HJ-1A CCD	2010-02-05 02:44	-167.9
44	HJ-1B CCD	2009-01-18 02:42	-120.5	89	HJ-1B CCD	2009-07-25 02:34	-173.5	134	HJ-1B CCD	2010-02-19 02:55	-211.5
45	HJ-1A CCD	2009-01-28 02:49	-144.8	90	HJ-1A CCD	2009-07-26 02:58	-185.0	135	HJ-1A CCD	2010-02-21 02:54	-176.6

<sup>a</sup>The imaging moment is Greenwich Mean Time (GMT)

<sup>b</sup>Water level is of the Jianggang Tidal Gauge Station (datum: mean sea level)

Landsat Thematic Mapper (TM), EO-1 Advanced Land Imager (ALI), SPOT High Resolution Visible (HRV), IRS-P6 Linear Imaging Self-Scanning Sensor (LISS), IRS-P6 Advanced Wide-Field Sensor (AWiFS), CBERS-1/2 CCD, Beijing-1 CCD, and ERS-2 SAR (Table 1). The spatial resolution of these satellite images varies from 10 m to 56 m. All satellite images are cloud-free, and the waterlines can be clearly identified. Few synchronous validation data were available for 2009 and 2010 due to changing weather conditions, regional geomorphology variations, and complex hydrodynamic environments. Therefore, DEMs derived from these non HJ-1 images were validated by the LiDAR and ground survey data, in order to show the feasibility of seasonal tidal flat DEM construction.

- (5) **Pre-processed auxiliary data.** Topographic maps (1:50,000) were used as base maps. Sea charts covering the South Yellow Sea (1:100,000), and the East China Sea (1:250,000) were used to facilitate water level simulation.

### HJ-1 Images Availability Analysis

To better reflect tidal flat topographic details, the WDM requires as many satellite images as possible. Moreover, only cloud-free images with clearly distinguishable waterlines can be used for tidal flat DEM construction, which typically indicate calm weather conditions. HJ-1 images were summarized into the following categories by manual visual evaluation: (1) high-quality (cloud-free and with clear waterlines); (2) high-quality but not completely cover the study area; (3) high-quality and the peripheral sandbanks are submerged totally; (4) medium-quality (sandbanks are partly covered by clouds); (5) poor-quality because of blurring; (6) poor-quality because of heavy clouds. Then, the numbers of various categories were counted on a month basis to analyze the availability of HJ-1 images for constructing seasonal tidal flat DEMs.

### Tidal Flat DEM Construction

To analyze the seasonal pattern of tidal flat, the first step is the topographic mapping for a serial of time, and then constructed DEMs were compared by time to identify seasonality. The rationale of the WDM is relatively simple: the waterline in the intertidal zone moves back and forth as the tides rise and fall. The WDM treats the waterline observed in remotely sensed images as an altimeter, the height of which can be derived from tide gauge data in situ or from a tidal level simulation result (Mason et al. 1995, Lohani and Mason 1999). A set of waterlines during different tidal periods can be retrieved from remotely sensed images to

construct a DEM. In this study, tidal flat DEMs construction can be divided into the following steps:

- (1) **Satellite image geo-correction.** All RS images were geometrically rectified to the Universal Transverse Mercator North zone 51 (UTM 51N) using the WGS 1984. The final total root mean square error during rectification was less than 0.5 pixels for each image. All images were resampled to a cell size of 30 m.
- (2) **Waterline extraction.** Two different waterline extraction methods are adopted in this study to deal with different datasets: the threshold segmentation for the HJ-1 images and the onscreen waterline digitization for all other satellite images. The *OTSU* threshold segmentation method was chosen to extract waterlines from a large number of HJ-1 images (Otsu 1979) because of its popularity (Sezgin and Sankur 2004). This method first develops the Normal Differential Water Index (NDWI) images by enhancing the contrast between water and other land cover types in the HJ-1 images. Then, this method separates water from background in each NDWI image. The resultant binary images (land/water) were converted to vector features as the boundaries between water and land (i.e. waterlines) semi-automatically. Manual corrections were made to improve the accuracy of the final result, including the elimination of incorrect waterlines, supplementing missing waterlines, and linking discontinuous waterlines. These manual corrections resulted in a positional error of the final results no greater than one pixel. For other satellite images, the true waterline position can be easily identified on the near infrared bands (Ryu et al. 2002). Therefore, to facilitate the delineation of the water-land boundary, the optimal band combinations for optical images were selected as follows: Landsat TM (R4,G3,B2), SPOT HRV (R3,G2,B1), CBERS-2 CCD (R4,G3,B2), IRS-P6 AWiFS/LISS (R4,G3,B2), EO-1 ALI (R7,G6,B5), and Beijing-1 CCD (R3,G2,B1). In addition, waterlines within the internal sandbank around tidal creeks were not considered in the analysis.
- (3) **Water level simulation.** The water elevation is obtained using a marine hydrodynamic simulation model in this study. The depth-averaged continuity equation based on spherical coordinates was used in the marine hydrodynamic model (Liu et al. 2012). To solve the continuity equation, an alternating direction implicit finite difference method was adopted based on nested models (Fig. 2). The nested models include two scales: a coarse model (of  $162 \times 205$  cells, covering the East China Sea, with a spatial resolution of  $4' \times 4'$ , Fig. 2a) and a fine model (of  $171 \times 202$  cells, covering the Jiangsu middle coast, Fig. 2b). The bathymetry of the two models was

- created using triangular interpolation. The two models are driven by harmonic constants (Chen et al. 2009). The closed boundaries (between water and land) are assumed to satisfy the no-discharge condition, while the open ones (between different water segments) are driven by tidal harmonic constants. For the coarse model, harmonic constants of eight major tidal constituents ( $M_2$ ,  $S_2$ ,  $N_2$ ,  $K_2$ ,  $K_1$ ,  $O_1$ ,  $P_1$  and  $Q_1$ ) for the open boundaries were calculated point-by-point using the bilinear interpolation method from the regional model around Japan (with a spatial resolution of  $5' \times 5'$ ). For the fine model, harmonic constants of major tidal constituents at the open boundaries were calculated from the coarse model simulation results (at 1-h intervals). The hydrodynamic model was run under the Delft 3D Flow module (WL|Delft Hydraulics, [<http://www.deltaresystems.com>]), and the water levels were simulated at 5-min intervals. The accuracy of the simulation results is approximately 30 cm. More details about the model calibration and validation can be found in the work of Chen et al. (2009) and Liu et al. (2012).
- (4) **Linking the water elevation to the waterline points.** All waterlines were resampled to points at 30 m intervals in order to facilitate matching up the water level simulation results with the waterlines at a specific time. The water level simulation was carried out at 5-min time intervals, and each waterline was matched with the closest simulation result. If the time at which a specific satellite image was recorded did not match exactly to these 5-min intervals, a snapshot of the water level at the specific time was calculated cell-by-cell using a linear interpolation of the two succeeding water level simulation results (Liu et al. 2012). In the finer grid, the resolution of the outside cells closer to the open boundaries is approximately  $5 \times 5$  km, while the resolution of the inside cells closer to land, is approximately  $200 \times 200$  m. In order to avoid unnatural breaks in elevation at the borders of the cells (Heygster et al. 2010), the elevation values are interpolated to a finer grid with a cell size of 30 m. The relatively small variability in the gradient of the water-surface topography allows the use of a simple bilinear interpolation method. Effectively this approach means that the tidal height of each discrete waterline point was interpolated and labeled according to the water level simulation results obtained at the time of satellite overpass. In order to create a single DEM for a particular season, all waterline points within a specific time period (e.g. 3 months) were merged into a single waterline point dataset.
  - (5) **Creating tidal flats DEMs from heightened waterline point dataset.** Waterlines in multi-temporal satellite images may cross each other, especially where the tidal

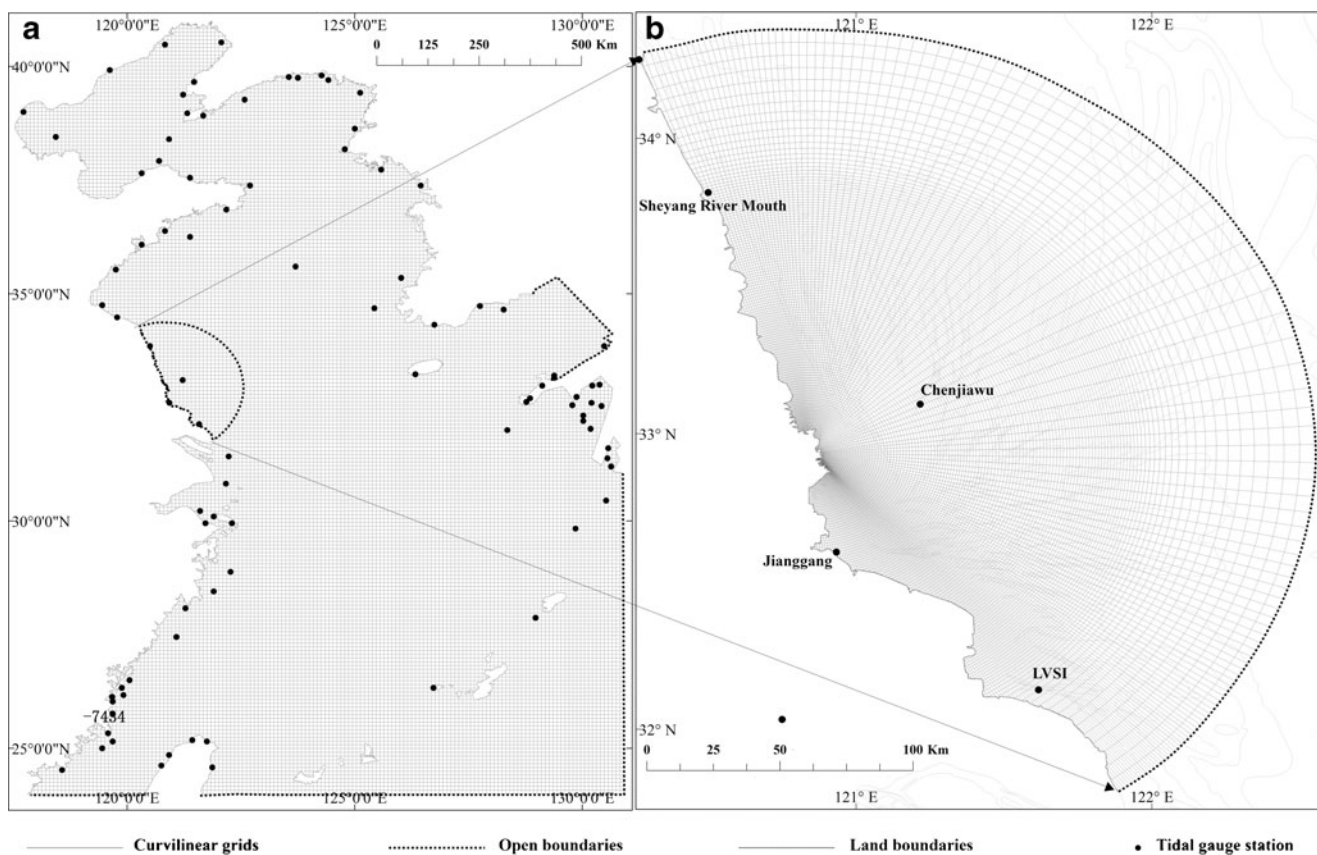


**Fig. 2** Nested models of the study area. **a** Bathymetry of the East China Sea superimposed with the coarse model and **(b)** bathymetry of the South Yellow Sea superimposed with the fine, staggered curvilinear grid

lands are quite low. This may be the result of real topographic changes or small-scale variations in hydrodynamic conditions. Median filtering was applied to the waterline point dataset to reduce the effect of this noise. More details about the median filtering algorithm are

reported by Liu et al. (2013). In general, grid-based DEMs preserve morphological information better than Triangulated Irregular Networks (TINs) (Jaakkola and Oksanen 2000). The grid-based DEM was therefore selected as the most appropriate data structure for the terrain

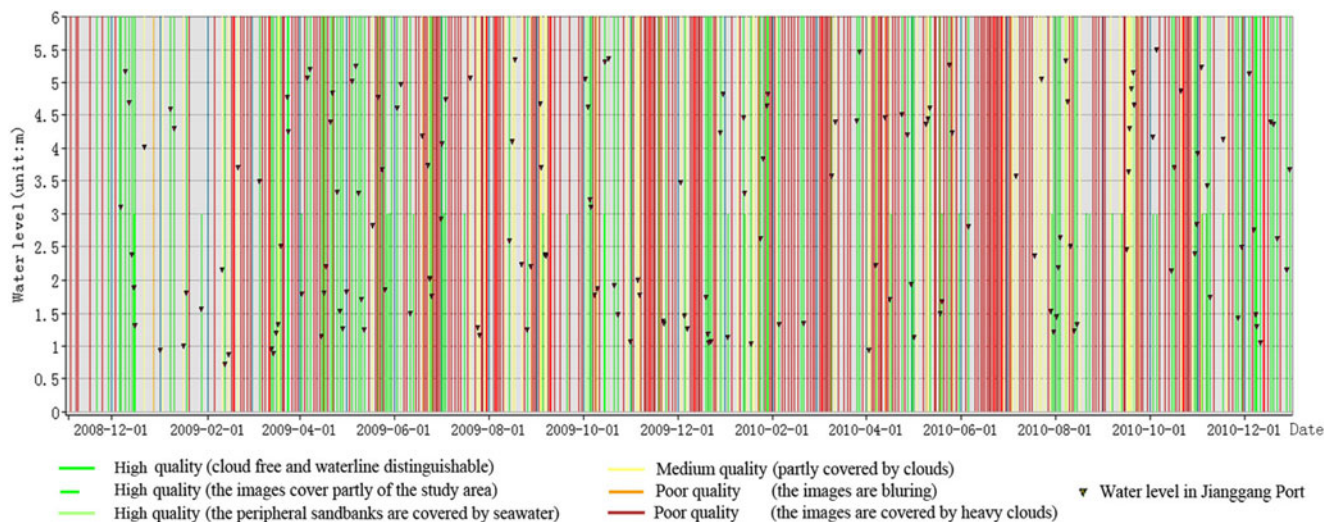


**Fig. 3** Usability of multi-phase HJ-1 optical images acquired from November 2008 to December 2010. Each green vertical line represents a high-quality image while ochre and red vertical lines represent images of insufficient quality

**Table 2** Eight DEMs of the Jiangsu middle coast retrieved from satellite images in this study

No.	Time Period	Season	Amount of satellite images	Area of exposed tidal flats (km <sup>2</sup> )
1	March to May, 2006	Spring	13	1913.95
2	March to May, 2008	Spring	12	1685.04
3	October to December 2008	–	14	1450.22
4	December 2008 to February 2009	Winter	18	1597.28
5	March to May 2009	Spring	29	1776.25
6	June to August 2009	Summer	18	1485.99
7	September to November 2009	Autumn	18	1339.81
8	December 2009 to February 2010	Winter	21	1664.21

models of the tidal flats in this study. The cell size of the DEMs was set to 60 m, based on the fact that the resolution of the satellite images used in the analysis varied from 10 to 56 m. A gridded DEM was created from the waterline point dataset using bilinear interpolation.

#### Tidal Flat Seasonal Pattern Analysis

The seasonal cycles of tidal flats can be indicated by the terrain variations. In our study, a time series of seasonal tidal flat DEMs were constructed, and the volume of tidal flat was employed as the indicator for quantitatively analyzing the seasonal terrain variations, and thus the season pattern of tidal flats. Furthermore, considering the variation of the exposed area of tidal flat DEMs in different periods, the sharing boundaries of these seasonal DEMs was extracted firstly to ensure the comparability. Then, the tidal flat volumes in the public region are calculated by multiplying the area (3,600 m<sup>2</sup> each cell in this study) and the height at a given elevation intervals (10 cm intervals is adopted in this study). All the above operations are executed by ArcGIS software (ESRI, [<http://www.esri.com>]).

## Results

#### Usability of HJ-1 Images for Constructing Seasonal Tidal Flat DEMs

From November 4, 2008, to December 31, 2010, a total of 455 optical images covering the Jiangsu middle coast were recorded by the HJ-1 A/B satellites. This represents approximately one optical image every 1.73 days. A total of 117 images were of high-quality, representing 25.7 % of the original 455 images. Of these 117 usable images 60 were collected by the HJ-1A satellite and 57 by the HJ-1B satellite. The other 338 images were considered of insufficient quality: 227 images were excluded because of heavy clouds, 79 images were excluded because of partial cloud coverage,

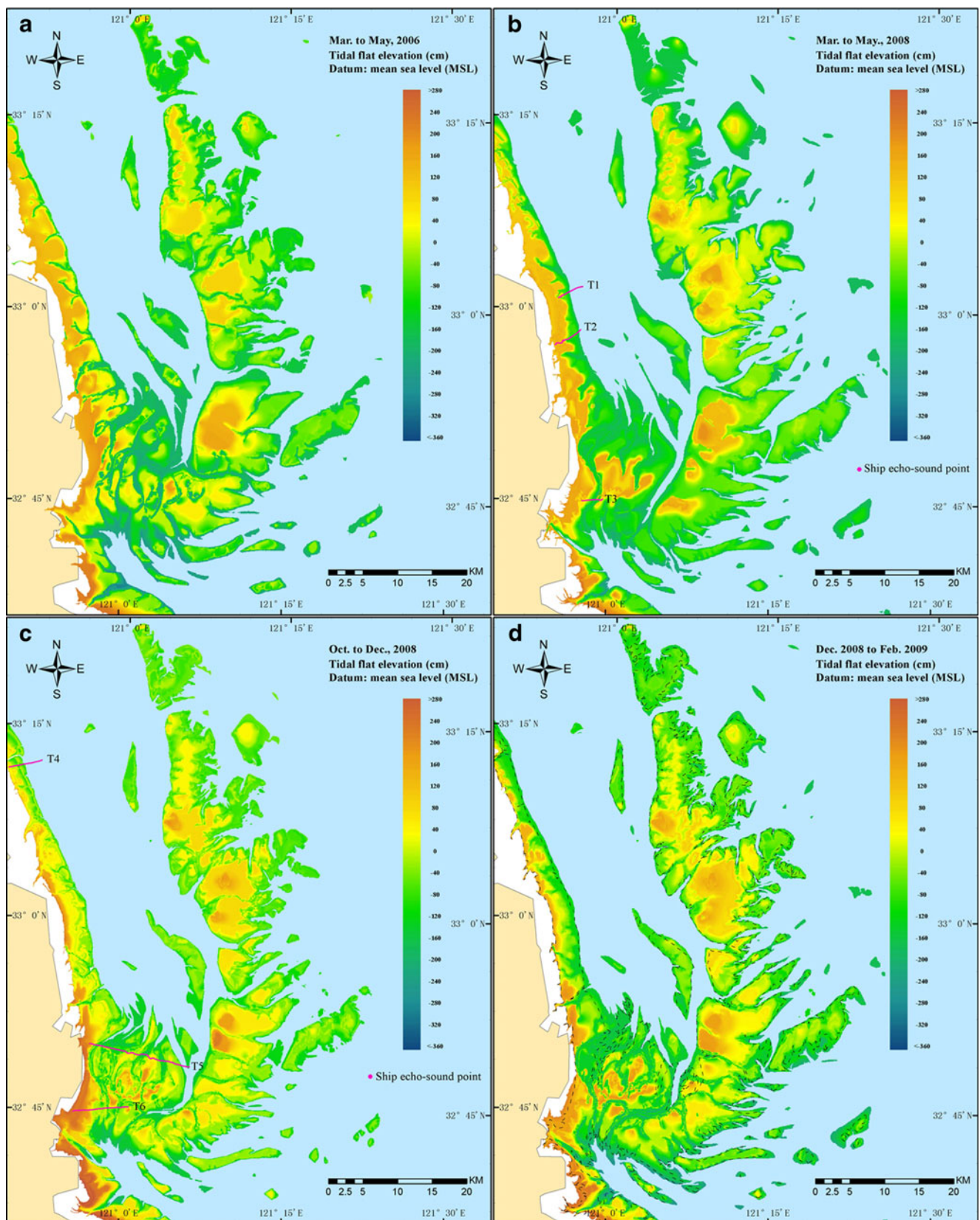
28 images were excluded because they did not completely cover the study area, and 4 images were excluded because of blurriness. The usability of the HJ-1 images from 2008 to 2010 is represented in Fig. 3. In general, there are more high-quality images in Winter (from December to February) than in Summer (from June to September). This is because the poor weather caused by the Jiang-huai quasi-stationary front (in June and July) greatly impacts the optical image quality. However, even in Summer there are enough HJ-1 images of acceptable quality (18 in total) to create DEMs of the tidal flat.

#### Seasonal Tidal Flat DEMs and Accuracy Assessment

Using the WDM approach, a total of eight DEMs of the tidal flats of the Jiangsu middle coast were created, each representing the topography for a three month time period (Table 2, Fig. 4a–h). The specific numbers of images for each DEM are listed in Table 2. The first three DEMs used medium-resolution satellite images from various sources, while the last five DEMs used HJ-1 images. Figure 4a–c shows the range of elevation from –3.6 to +2.4 m above mean sea level (MSL) in the study area. Overall, the maps accurately present the large-scale topography. Important topographic features like sandbanks and tidal channels can be identified in all of these maps and are positioned precisely, and the horizontal gradients also appear to be positioned correctly. Table 2 reports the exposed tidal flat areas in each DEM. The differences in these areas are likely due to variations in the minimum water level at the time the images were recorded.

**Fig. 4** DEMs of the Jiangsu middle coast from March 2006 to February 2010. **a** March to May, 2006; **b** March to May, 2008; **c** October to December, 2008; **d** Winter 2008 (December 2008 to February 2009); **e** Spring 2009 (March to February, 2009); **f** Summer 2009 (June to August, 2009); **g** Autumn 2009 (September to November, 2009); and **h** Winter 2009 (December 2009 to February 2010). Land areas are shown in beige, ultra-tidal flats in white and deep water in light-blue. T<sub>1</sub>–T<sub>6</sub> in (**b**) and (**c**) are six transects measured in March to May, October to December 2008. Dashed lines in (**d**)–(**h**) show the intersecting boundaries of the five tidal flat DEMs





Limited validation data were available for 2009–2010, and as a result the 2006 LiDAR DEM and six-transect survey

data were used to determine the accuracy of DEMs in the corresponding time period. To assess the DEMs for Spring

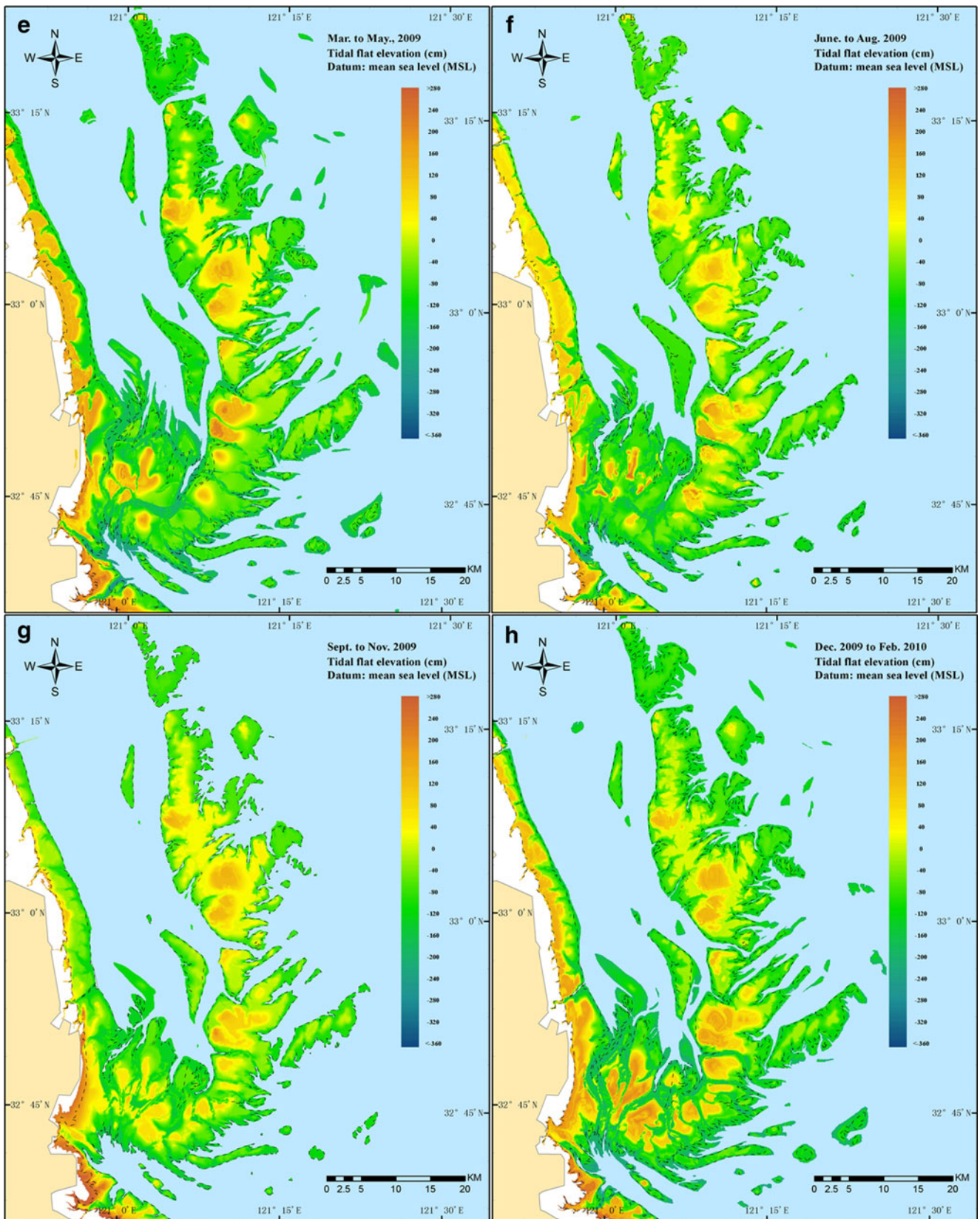


Fig. 4 (continued)

2006 (Fig. 4a), the 2006 LiDAR DEM was resampled to 60 m (Fig. 5a) in order to match the resolution of the created DEMs of tidal flats. An error map was created by calculating the difference between these two DEMs (Fig. 5b). The mean error for the study area is 45.13 cm. 83 % of the cells the Spring 2006 DEM have an error of less than 40 cm compared to the LiDAR DEM. Along tidal creeks with relatively steep slopes the error is up to 1.5 m, forming a linear shape as the area being circled by red dash line in Fig. 5b. The vertical accuracy of the Spring 2006 DEM is quite good given the limited number of satellite images and the relatively coarse resolution of these images.

Three transects collected in April and May 2008 (magenta points in Fig. 4b), and three transects collected in October 2008 (magenta points in Fig. 4c) were used to determine the accuracy of the tidal flat DEMs for those seasons. Figure 6a–f show a direct comparison between the transect data collected in the field and the transects derived from the tidal flat DEMs. The mean error for all six transects is less than 45 cm. For the DEM (March to May, 2008), the mean errors for the three profiles ( $T_1$ ,  $T_2$ , and  $T_3$  in Fig. 3b) are 30.29, 33.55, and 34.35 cm, respectively. For the DEM (October to December, 2008), the mean errors for the three profiles ( $T_4$ ,  $T_5$ , and  $T_6$  in Fig. 4c) are 29.31, 41.93, and 40.34 cm, respectively.

## Seasonal Patterns in Tidal Flat Topography Based on HJ-1 Images

Five DEMs (Fig. 4d–h) derived from HJ-1 images were used to calculate the tidal flat volume for seasonal pattern analysis. Figure 7 shows the five seasonal tidal flat volume curves at 10 cm elevation intervals. Comparing the five seasonal volume curves in Fig. 7a, we can find that a seasonal erosion-and-deposition cycle from Winter 2008 to Winter 2009—the tidal flats are in erosion from Winter 2008 to Summer 2009, while in deposition from Summer 2009 to Winter 2009. Furthermore, the intra-annual pattern are reflected by the intersected volume curves of Winter 2008 (red points) and Winter 2009 (magenta points) at ~10 cm above MSL (Fig. 7a), which indicates that the low tidal flats (<10 cm above MSL) are in erosion, while the high tidal flats (>10 cm above MSL) are in deposition. Besides, each sandbank has a specific erosion-and-deposition cycle (Fig. 7b–f):

- (1) **The Dongsha Sandbank** (Fig. 7b). Tidal flats in this sandbank experience a typical erosion-and-deposition cycle—the tidal flats are in erosion from Winter 2008 to Summer 2009, while in deposition from Summer 2009 to Winter 2009. Moreover, comparing the volume

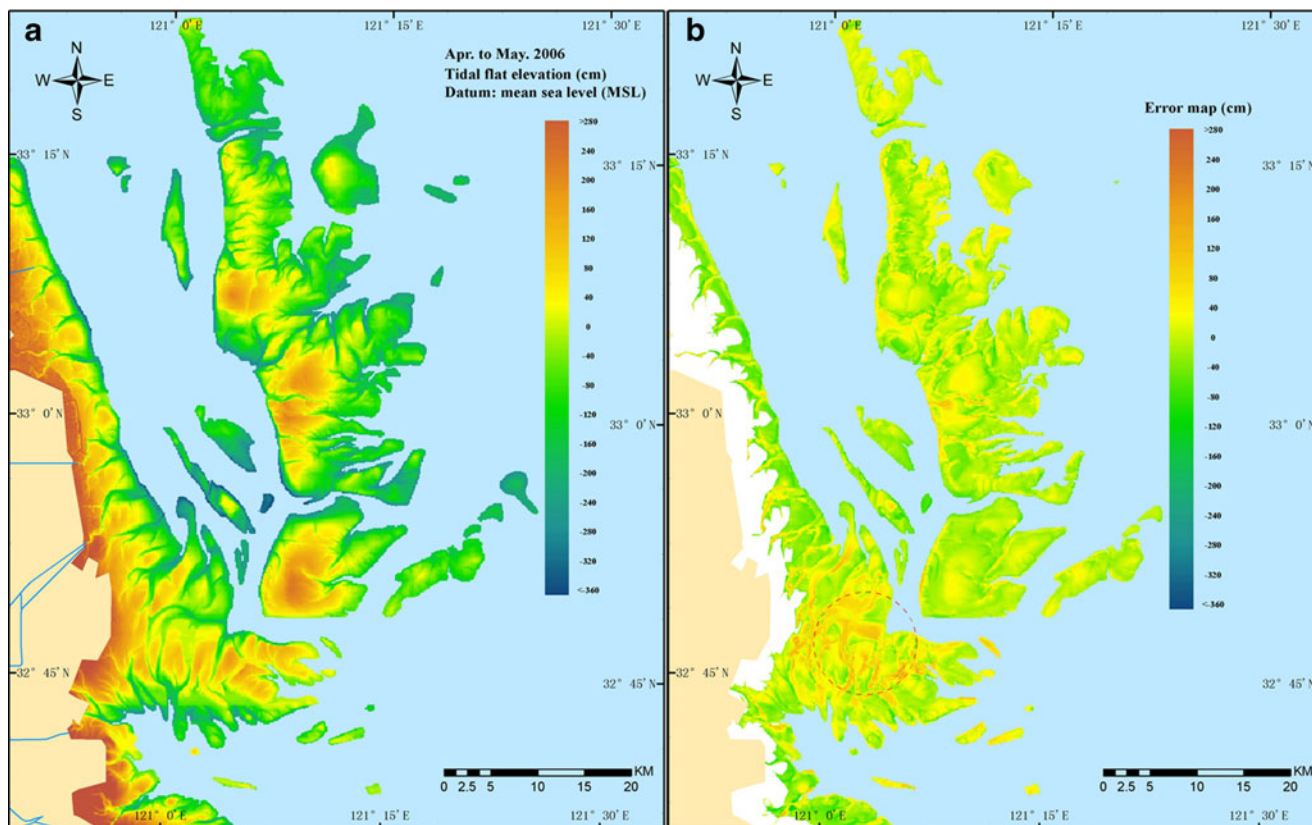


**Fig. 5** DEM and error map: **a** Tidal flat LiDAR DEM of Jiangsu middle coast (measured in April and May, 2006); **b** error map based on a comparison of Fig. 4a and the 2006 LiDAR DEM

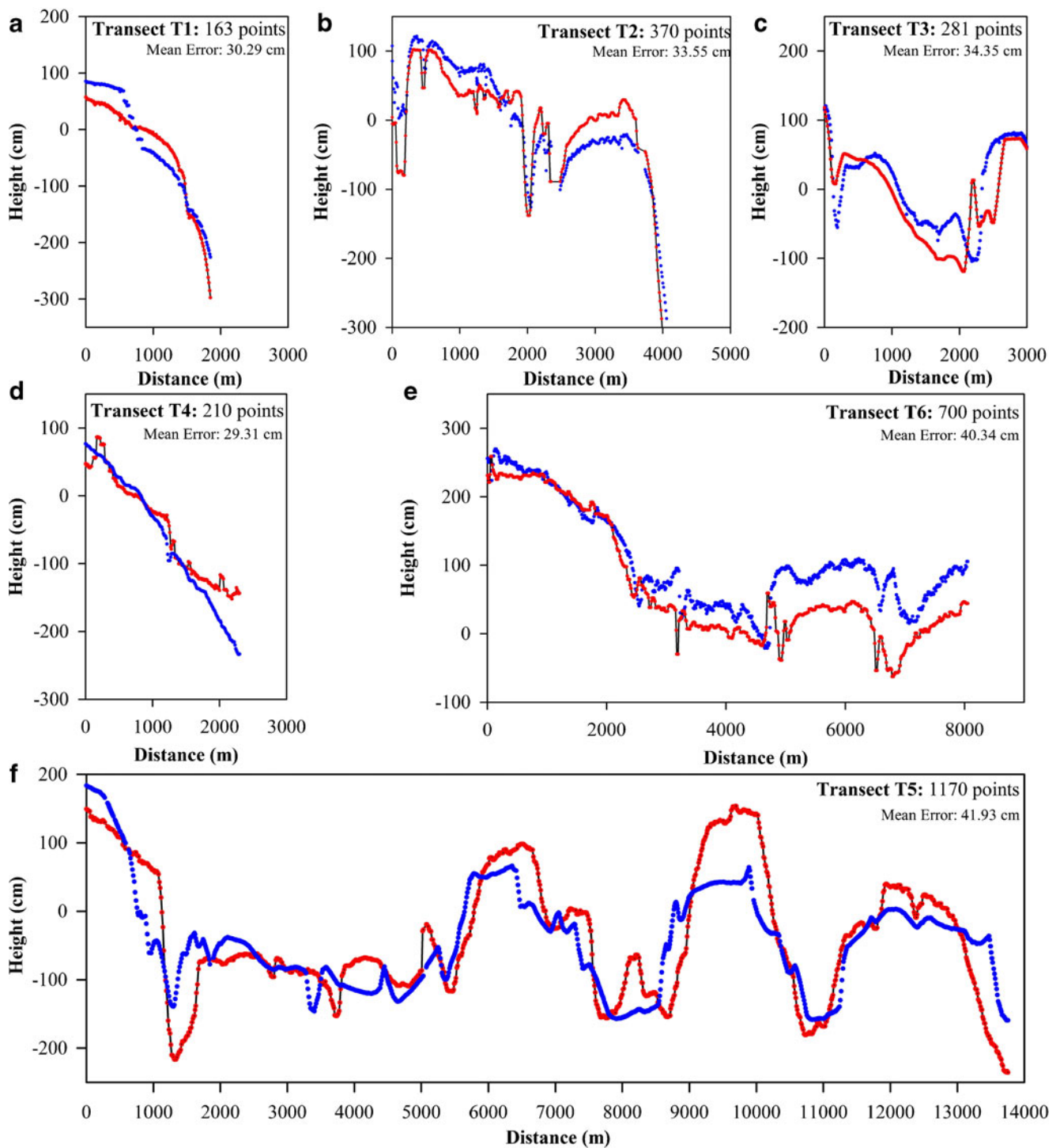


**Fig. 6** Comparison of transects: **a**  $T_1$  in Fig. 4b; **b**  $T_2$  in Fig. 4b; **c**  $T_3$  in Fig. 4b; **d**  $T_4$  in Fig. 4c; **e**  $T_6$  in Fig. 4c; **f**  $T_5$  in Fig. 4c

curves of Winter 2008 (red points) and Winter 2009 (magenta points), this sandbank reveals an erosion intra-annual pattern during this period (Fig. 7b).

- (2) **The Liangyuesha and Niluoheng Sandbanks** (Fig. 7c and d). These two small sandbanks are in the peripheral of the Dongsha Sandbank, showing an atypical erosion-and-deposition cycle—the tidal flats are drastically

- eroded from Winter 2008 to Autumn 2009, while slightly recovered from Autumn 2009 to Winter 2009.
- (3) **The Tiaozini, Gaoni, and Jiangjiasha Sandbanks** (Fig. 7e). These three inner sandbanks show similar seasonal patterns with the Dongsha Sandbank. However, these three sandbanks reveal a deposition intra-annual pattern from Winter 2008 to Winter 2009 (Fig. 7e).

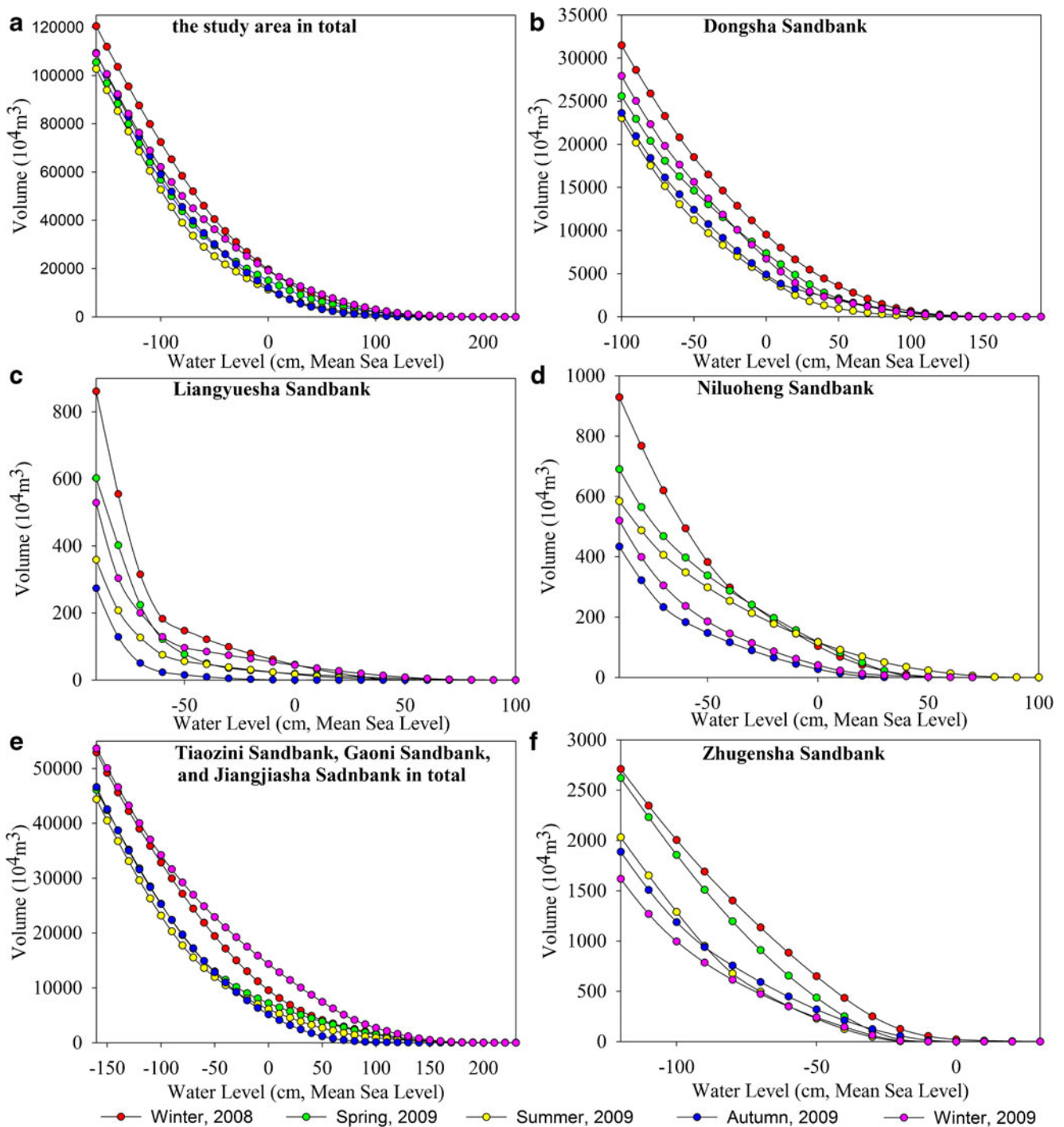


**Fig. 7** Seasonal patterns of tidal flats of the Jiangsu middle coast: **a** entire study area; **b** Dongsha Sandbank; **c** Liangyuesha Sandbank; **d** Niluoheng Sandbank; **e** Tiaozini, Gaoni, and Jiangjiasha Sandbanks; **f** Zhugensha Sandbank

Higher tidal flat areas reveal more deposition, which is in contrast with the results for the Dongsha Sandbank.

- (4) **The Zhugensha Sandbank** (Fig. 7f). The Zhugensha Sandbank is a peripheral sandbank of the Tiaozini, Gaoni, Jiangjiasha sandbank, and its tidal flats do not reveal an erosion-and-deposition cycle—the tidal flats are in erosion from Winter 2008 to Winter 2009.

## Discussion

Limitations of the WDM for Seasonal Pattern Analysis

The present study has illustrated that the WDM approach using a time-series of HJ-1 A/B images can be used to create seasonal DEMs for large areas of tidal flats. Seasonal

variations in the tidal flat topography can be derived from these seasonal DEMs. However, the tidal flat DEMs may not be very accurate in certain intertidal zones. One of the assumptions of the WDM approach is that the waterline in a given satellite image indicates the water-land-boundary at a particular time. This includes three types of information: (1) the location ( $x, y$ ) of the water-land-boundary; (2) the water depth information ( $d$ ) along this boundary (generally speaking, the water depth is zero); (3) the water height information ( $h$ ) along this boundary according to a given height datum. However, in some special intertidal zones, the water depth information or the water height information of the waterlines may not be reliable. Two specific zones are discussed below.

- (1) **Salt-marshes.** High-density salt-marshes (e.g., *Spartina alterniflora* salt-marsh, Fig. 8) are widely distributed in the mid-upper intertidal zone of the Jiangsu coast (Zhang et al. 2004). The height of *Spartina alterniflora* salt-marshes in the Jiangsu middle coast is approximately 1.5 m on average, although sometimes as high as 2–3 m (Zhou et al. 2009). If the satellite image is recorded during the high tide period, the edge of the immersed salt-marsh (water-vegetation boundary) could incorrectly be identified as the waterline since the actual water-land boundary is typically covered by the high-density salt-marshes. As a result, errors in these salt-marsh areas may be introduced to the tidal flat DEMs. In the present study, all water-vegetation boundaries were removed manually. As a result, the tidal flat DEMs exclude salt-marshes, even though they are parts of upper intertidal flats.
- (2) **Tidal flat depression areas.** The well-developed tidal creek systems in the Jiangsu middle coast exhibit a strong self-adjustment capacity to maintain their morphological stability (Zhang 1995). These tidal creeks tend to erode laterally, with lateral migration of up to



**Fig. 8** *Spartina alterniflora* salt-marshes outside the Chuandong River Dam

5 km in a month. In addition, tidal catchment basins with underwater barriers are commonly found in the upstream regions of these tidal creeks (which are also in the mid-upper intertidal zone). In these tidal flat depression areas, the upstream catchment basins may be filled with sea-water during inundation, and water remains in these sinks at a higher level than the general sea level during low tides. Waterlines of these depression areas during low tides do not accurately reflect the true sea-level. In the present study, waterlines of tidal creeks were removed, which in itself may introduce a certain amount of error (e.g. the area marked with a red circle in Fig. 5b).

#### Causes of Tidal Flat Seasonal Pattern

Two factors may interact to create the erosion-and-deposition cycles observed in the Jiangsu middle coast region: sediment supply and high frequency of severe tropical storms during Summer and Autumn. Field observations have shown that sediment supply from the Abandoned Yellow River Delta in the northern Jiangsu coast and peripheral sandbanks are the main source of sediment for the inner sandbanks in the Jiangsu middle coast region (Gao et al. 2011; Wang et al. 2012b; Zhang and Chen 1992). Despite the influence of severe tropical storms, the patterns of the tidal flats of the inner sandbanks (such as the Dongsha, Tiaozini, Gaoni and Jiangjiasha Sandbanks) show a balanced erosion-and-deposition cycle or a surplus sediment flux. This is the result of the barrier provided by the peripheral sandbanks and a sufficient sediment supply. However, the peripheral sandbanks (such as the Liangyuesha, Niluoheng and Zhugensha Sandbanks) show an atypical erosion-and-deposition cycle, resulting in an overall negative sediment flux.

It is important to note that these rhythmical seasonal patterns are derived from satellite images. Additional evidence is needed to confirm these findings, including more frequent satellite observations (e.g., sufficient number of satellite snapshots before and after severe tropical storms), long-term sustained hydraulic in situ, and surface sediment sampling.

#### Conclusions and Outlook

The topography of tidal flats is highly dynamic, both spatially and temporally. The current research analyzes the seasonal patterns of tidal flats using optical images from the Chinese HJ-1 A/B satellites. The two major conclusions of the research are as follows:

- (1) The accuracy assessment indicates that the average vertical error in the seasonal DEMs is approximately

45 cm. Given the dynamic nature of the tidal flats of the Jiangsu middle coast, the HJ-1 images could be a qualified source to produce satisfactory tidal-flat DEMs with high spatio-temporal resolution and acceptable vertical accuracy.

- (2) The erosion-and-deposition cycle of the tidal flats was characterized using five seasonal DEMs derived from HJ-1 optical imagery. Results indicate a clear erosion-and-deposit cycle of the tidal flats in the Jiangsu middle coast, with deposition during the Winter and erosion during the Summer.

The current study illustrates that the seasonal DEMs of tidal flats can be constructed using HJ-1 images. Actually, more and more earth observation satellites have been launched or to be launched. The additional imagery from these satellites makes it possible to improve the temporal resolution of the tidal flat DEMs. For example, the ZY1-02C satellite (launched on December 22, 2011, with a 5-day revisit cycle), the ZY-3 satellite (launched on January 9, 2012, with a 5-day revisit cycle), and the Shi-Jian 9A/B satellites (launched on October 14, 2012), have recently been launched. Based on the conjunction of HJ-1 images and space-borne images taken by the aforementioned satellites, the temporal resolution of the tidal flat DEMs will be shortened to 1 month.

In addition, the European Aeronautic Defense and Space Company (EADS), is establishing a constellation of four satellites, phased 90° apart in the same helio-synchronous quasi polar orbit, which is similar to the HJ-1 satellite constellation. This new constellation consists of Pléiades 1A (launched on December 17, 2011), SPOT-6 (launched on September 9, 2012), Pléiades 1B (launched on December 2, 2012), and SPOT-7 (to be launched in 2014). It will provide high-resolution images (1.5 m) and very-high-resolution images (0.5 m) in as little as 6 h. It is expected that products based on such high temporal and spatial resolution images will offer much more detailed information for research on seasonal cycle of tidal flats.

**Acknowledgments** This research is supported by the National Natural Science Foundation of China (NO. 41171325, NO. 40701117, NO. 41230751, and NO. J1103408), the Program for New Century Excellent Talents in University (NCET-12-0264), the National Key Project of Scientific and Technical Supporting Programs funded by the Ministry of Science & Technology of China (NO. 2012BAH28B02), the Fundamental Research Funds for the Central Universities and PAPD (Priority Academic Program Development of Jiangsu Higher Education Institutions). The authors are grateful to the China Center for Resource Satellite Data and Applications (CRESDA) for providing the CBERS CCD, HJ-1A/B optical images, to the Center for Earth Observation and Digital Earth (CEODE, China) for providing the IRS-P6 LiSS/AWiFS images, and to the Earth Resources Observation and Science Center (EROS, USA) for providing the EO-1 ALI images. The authors are also grateful for the valuable tidal flat transects data provided by Dr. Xianrong Ding (Hohai University, HHU). Any errors or shortcoming in the paper are the responsibility of the authors.

## References

- Blott SJ, Pye K (2004) Application of lidar digital terrain modelling to predict intertidal habitat development at a managed retreat site: Abbots Hall, Essex, UK. *Earth Surface Processes and Landforms* 29:893–905
- Cai WW, Song JL, Wang JD, Xiao ZQ (2011) High spatial-and temporal-resolution NDVI produced by the assimilation of MODIS and HJ-1 data. *Canadian Journal of Remote Sensing* 37:612–627
- Chen LC, Rau JY (1998) Detection of shoreline changes for tideland areas using multi-temporal satellite images. *International Journal of Remote Sensing* 19:3383–3397
- Chen JY, Cheng HQ, Dai ZJ, Eisma D (2008) Harmonious development of utilization and protection of tidal flats and wetlands - a case study in Shanghai area. *China Ocean Engineering* 22:649–662
- Chen KF, Wang YH, Lu PD, Zheng JH (2009) Effects of coastline changes on tide system of Yellow Sea off Jiangsu coast, China. *China Ocean Engineering* 23:741–750
- Gao S, Wang YP, Gao JH (2011) Sediment retention at the Changjiang sub-aqueous delta over a 57 year period, in response to catchment changes. *Estuarine, Coastal and Shelf Science* 95:29–38
- Heygster G, Dannenberg J, Notholt J (2010) Topographic mapping of the German tidal flats analyzing SAR images with the waterline method. *IEEE Transactions on Geoscience and Remote Sensing* 48:1019–1030
- Jaakkola O, Oksanen J (2000) Creating DEMs from contour lines: Interpolation techniques which save terrain morphology. *GIM International* 14:46–49
- Lemke A, Lunau M, Stone J, Dellwig O, Simon M (2009) Spatio-temporal dynamics of suspended matter properties and bacterial communities in the back-barrier tidal flat system of Spiekeroog Island. *Ocean Dynamics* 59:277–290
- Liu YX, Li MC, Cheng L, Li FX, Shu YM (2010) A DEM inversion method for inter-tidal zone based on MODIS dataset: a case study in the Dongsha Sandbank of Jiangsu Radial Tidal Sand-Ridges, China. *China Ocean Engineering* 24:735–748
- Liu XJ, Gao S, Wang YP (2011) Modeling profile shape evolution for accreting tidal flats composed of mud and sand: A case study of the central Jiangsu coast, China. *Continental Shelf Research* 31:1750–1760
- Liu YX, Li MC, Cheng L, Li FX, Chen KF (2012) Topographic mapping of offshore sandbank tidal flats using the waterline detection method: a case study on the Dongsha Sandbank of Jiangsu Radial Tidal Sand Ridges, China. *Marine Geodesy* 35:362–378
- Liu YX, Li MC, Mao L, Cheng L, Li FX (2013) Toward a method of constructing tidal flat digital elevation models with MODIS and medium-resolution satellite images. *Journal of Coastal Research* 29:438–448
- Lohani B, Mason DC (1999) Construction of a digital elevation model of the Holderness coast using the waterline method and airborne thematic mapper Data. *International Journal of Remote Sensing* 20:593–607
- Mason DC, Davenport IJ, Robinson GJ, Flather RA, McCartney BS (1995) Construction of an intertidal digital elevation model by the ‘water-line’ method. *Geophysical Research Letters* 22:3187–3190
- Mason DC, Davenport IJ, Flather RA, Gurney C (1998) A digital elevation model of the inter-tidal areas of the Wash, England, produced by the waterline method. *International Journal of Remote Sensing* 19:1455–1460
- Mason DC, Gurney C, Kennett M (2000) Beach topography mapping: a comparison of techniques. *Journal of Coastal Conservation* 6:113–124
- Mason DC, Scott TR, Dance SL (2010) Remote sensing of intertidal morphological change in Morecambe Bay, UK, between 1991 and 2007. *Estuarine, Coastal and Shelf Science* 87:487–496

- Otsu N (1979) Threshold selection method from gray-level histograms. *IEEE Transactions on Systems, Man, and Cybernetics* 9:62–66
- Pino M, Busquets T, Brummer R (1999) Temporal and spatial variability in the sediments of a tidal flat, Queule River Estuary, south-central Chile. *Revista Geologica De Chile* 26:187–204
- Ryu JH, Won JS, Min KD (2002) Waterline extraction from Landsat TM data in a tidal flat - A case study in Gomso Bay, Korea. *Remote Sensing of Environment* 83:442–456
- Ryu JH, Kim CH, Lee YK, Won JS, Chun SS, Lee S (2008) Detecting the intertidal morphologic change using satellite data. *Estuarine, Coastal and Shelf Science* 78:623–632
- Sezgin M, Sankur B (2004) Survey over image thresholding techniques and quantitative performance evaluation. *Journal of Electronic Imaging* 13:146–168
- Wang Q (2012) Technical system design and construction of China's HJ-1 satellites. *International Journal of Digital Earth* 5:202–216
- Wang QA, Wu CQ, Li Q, Li JS (2010) Chinese HJ-1A/B satellites and data characteristics. *Science China-Earth Sciences* 53:51–57
- Wang Y, Zhang YZ, Zou XQ, Zhu DK, Piper D (2012a) The sand ridge field of the South Yellow Sea: origin by river-sea interaction. *Marine Geology* 291:132–146
- Wang YP, Gao S, Jia JJ, Thompson CEL, Gao JH, Yang Y (2012b) Sediment transport over an accretional intertidal flat with influences of reclamation, Jiangsu coast, China. *Marine Geology* 291:147–161
- Wimmer C, Siegmund R, Schwabisch M, Moreira J (2000) Generation of high precision DEMs of the Wadden Sea with airborne interferometric SAR. *IEEE Transactions on Geoscience and Remote Sensing* 38:2234–2245
- Woolard JW, Colby JD (2002) Spatial characterization, resolution, and volumetric change of coastal dunes using airborne LIDAR: Cape Hatteras, North Carolina. *Geomorphology* 48:269–287
- Xing F, Wang YP, Wang HV (2012) Tidal hydrodynamics and fine-grained sediment transport on the radial sand ridge system in the southern Yellow Sea. *Marine Geology* 291:192–210
- Zhang RS (1995) Equilibrium state of tidal mud flat, a case coastal area of central Jiangsu, China. *Chinese Science Bulletin* 40:1363–1368
- Zhang RS, Chen CJ (1992) Study of the evolution of Jiangsu offshore sandbanks and the prospects for tiaozini sandbanks merging into land. China Ocean Press, Beijing, pp 40–42
- Zhang RS, Shen YM, Lu LY, Yan SG, Wang YH, Li JL, Zhang ZL (2004) Formation of *Spartina alterniflora* salt marshes on the coast of Jiangsu Province, Spain. *Ecological Engineering* 23:95–105
- Zhao B, Guo H, Yan Y, Wang Q, Li B (2008) A simple waterline approach for tidelands using multi-temporal satellite images: a case study in the Yangtze Delta. *Estuarine, Coastal and Shelf Science* 77:134–142
- Zhou HX, Liu JE, Qin P (2009) Impacts of an alien species (*Spartina alterniflora*) on the macrobenthos community of Jiangsu coastal inter-tidal ecosystem. *Ecological Engineering* 35:521–528